Tidal motion enhancement around islands

by Zygmunt Kowalik[1] and Aleksey V. Marchenko[2]

ABSTRACT

Tidally-generated, trapped motions can significantly enhance and modify sea level and currents in the island proximity. The analytical solution for incident waves interacting with a cylindrical island with a circular sill has been constructed to investigate this phenomenon. To derive solutions for the scattering problems simple Sverdrup and Kelvin waves are used as incident waves. The amplification of the signal along the island perimeter has shown to be a function of frequency, relative dimensions of the island and the circular sill surrounding the island, relative sill depth, and the bottom friction. Although the incident diurnal tide may be amplified through the resonant response, this resonance occurs in the shallow water where the bottom friction damps the effect. The dispersion equation shows that the geometry of the problem favors amplification of semidiurnal tides. Analytical solutions obtained by superposition of the incident and scattered waves around an island are used to explain the observed peculiarities of tides in the vicinity of the Pribilof Islands, Bering Sea.

1. Introduction

Numerical calculations and field observations revealed tidally driven, trapped motions around certain islands (Larsen, 1977; Lee and Kim, 1993, 1999; Kowalik and Proshutinsky, 1995; Kowalik and Stabeno, 1999). Investigations of the tidal wave pattern lead to the conclusion that a tidal wave around an island is a superposition of two types of waves: a primary wave arriving from a distant source and secondary waves generated by the island. The primary wave consists of incoming propagating and reflected propagating waves. The secondary wave is trapped around the island and decays offshore from the island. While the primary wave influences sea level in the entire domain, the trapped wave affects only the island's vicinity, propagating clockwise (in the northern hemisphere) around the island with the same period as the primary wave. The distortion caused by the island modifies the amplitude of the tidal sea level, changes the time of the arrival of low and high tides, and enhances tidal currents.

Proudman (1914) investigated scattering of a tidal wave by small circular and elliptical islands (see also Figs. 149 and 150 in Defant 1960, vol. II). Larsen (1977) analyzed a systematic variation in amplitude and phase around the Hawaiian Islands and applied the solution of the scattering problem around an elliptical island to explain the observations.

---

1. Institute of Marine Science, University of Alaska, Fairbanks, Alaska, 99775, U.S.A. *email: ffzk@ims.uaf.edu*
2. General Physics Institute, Russian Academy of Sciences, Moscow, Russia.

Analytical solutions for the tidal wave scattering around small islands were further developed by Lee and Kim (1999) by introducing bottom friction. The presence of bottom friction enabled them to extend the scattering theory to subinertial frequencies. Their theory was corroborated by the observations taken around Cheju Island. This island, about 50 km in diameter, is located in Tsushima Strait between the Korean Peninsula and southern Japan at 33°30′N.

Observations and numerical computations by Kowalik and Proshutinsky (1995) around Bear Island in the Barents Sea, of approximately 20 km diameter, located at 74°30′N, and by Kowalik and Stabeno (1999) around the Pribilof Islands (the diameters less than 20 km), located at approximately 57N in the Bering Sea, delineated a dipole structure in the tidal sea level distribution. Maximum and minimum sea levels occur at the opposite sides of the islands. According to Proudman (1914) and Lee and Kim (1999) this feature depends on the direction of propagation of the incident wave relative to the island. From the point of view of an observer looking in the propagation direction of the incident wave, the tidal amplitude increases to the left and decreases to the right of the island. A linear wave (a wave with a straight crest) propagating from east to west should generate the local sea level maximum at the southern side of the island. In the Cheju Island region, the M_2 wave arrives from the east, therefore amplitudes are much larger on the southern side of this island than on the northern. In the Barents and Bering Seas the M_2 waves arrive from the west, setting the maximum amplitude at the northern shores of the islands. The interaction of tides and currents with the bottom topography around islands, often leads to current enhancement and, as a consequence, nonlinear interactions become stronger in such regions. Observations and model computations of the oscillatory tidal flow interacting with bottom topography demonstrate well developed rectilinear motion around banks and islands (Loder, 1980).

In this paper the previous analytical approach is developed in two directions. First we abandon the small island approximation used by Proudman (1914), Larsen (1977) and Lee and Kim (1999); but, more importantly, the variable bottom relief around islands is considered. This theory is applied to investigate the trapped tidal wave pattern around the Pribilof Islands in the Bering Sea. Although both islands have similar diameters, the observations show that the scattering phenomena is much stronger for the northern island (St. Paul Island) compared to the southern island (St. George Island). We search for explanations of this phenomenon in the occurrence of the broad shelf around St. Paul Island. In Figure 1 the depth distribution is coded by colors, and continuous lines denote the pattern of the amplitude of the M_2 tidal wave. Both islands are located on a shelf plain of approximately 80 m depth at some distance from the shelf break. The 50 m depth contour shows that St. Paul Island is surrounded by a wide area of shallow water extending 15–20 km beyond the island perimeter, while around St. George Island the shallow water extends only 3–5 km beyond the island perimeter. A tide wave enters the Bering Sea as a progressive wave from the North Pacific Ocean through the Aleutian passages (Sünderman, 1977; Pearson *et al.,* 1981; Kantha, 1995; Kowalik, 1999). The Pribilof Islands are
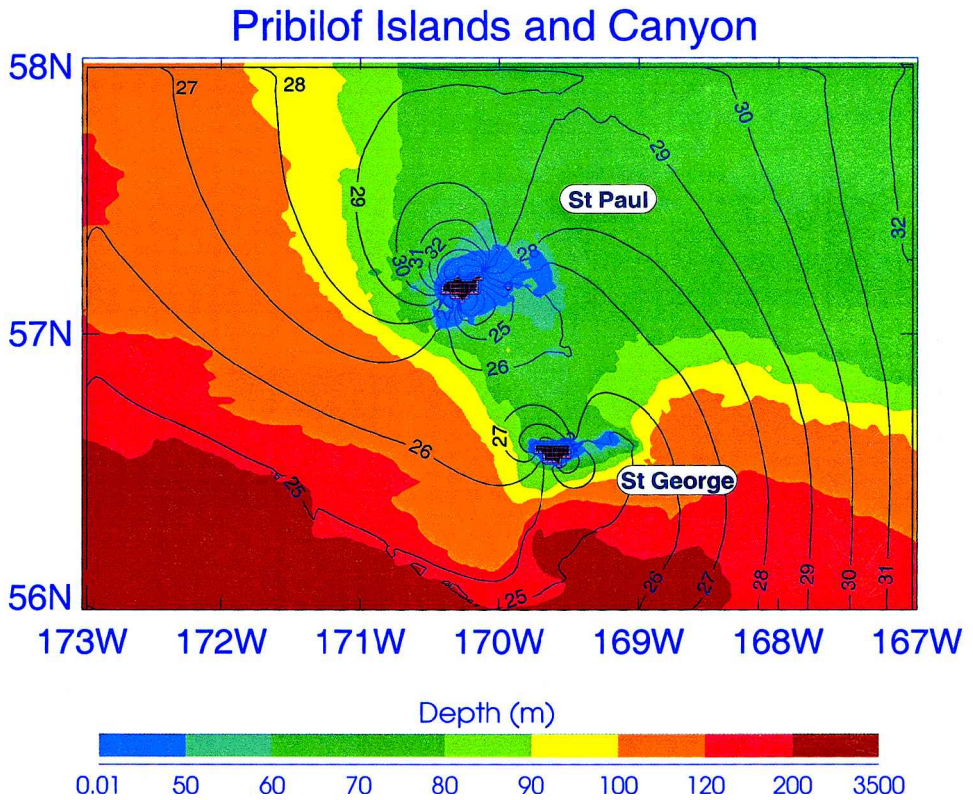
Pribilof Islands and Canyon

Figure 1. Amplitude (in cm) of the M_2 tide in the Pribilof Islands and Canyon domain. The depth is coded by colors. Based on Kowalik and Stabeno (1999).

located on the shelf, but close to the deep Bering Basin. Here tides propagate from the deep basin onto the shallow domain, which strongly enhances the tidal amplitudes and currents. The M_2 amplitude of the surface elevation is shown in Figure 1. It slowly changes from 24 cm in the deep basin to 31 cm over the open shelf. The sea level depicts the dipole structure around islands with the minimum located at the southeastern shores and the maximum at the northern shores. Especially conspicuous is the 14 cm sea level change across St. Paul Island. Around St. George Island the sea level change is only 7 cm. Due to topographic amplification by the shallow water, M_2 currents up to $50-70$ cm s^{-1} are generated around St. Paul Island (Kowalik and Stabeno, 1999). The driving mechanism which generates these strong currents around the islands is the dipole structure of the sea level (shown in Fig. 1) because the strength of the tidal stream is proportional to the sea level difference in the dipole structure.

The dynamics of diurnal tides can be described using the major constituent K_1. Although this wave has an amplitude of approximately 35 cm in the region of the Pribilof Islands, it does not generate the dipole structure of the same strength as the M_2 wave. The

difference in sea levels across St. Paul Island is only 5 cm and across St. George only 2 cm. Consequently, the diurnal currents are significantly smaller than semidiurnal currents (Kowalik and Stabeno, 1999).

The important difference in wave trapping around the Pribilof Islands is apparently related to the local topography, since both diurnal and semidiurnal tides are stronger at St. Paul Island. Observations also demonstrate that the different types of tides are enhanced in different ways, because at both islands the dipole structures are stronger for the M_2 wave, despite the fact that the amplitude of the incident K_1 wave being larger than the M_2 wave. To explain the peculiarities of tidal dynamics around the Pribilof Islands we may use a simple model of Sverdrup or Kelvin waves approaching the islands. As Mofjeld (1984) has suggested, the tidal waves in the Bering Sea shelf region resemble a Sverdrup wave generated by an incident wave from the Deep Bering Basin. The Sverdrup wave model predicts well the amplitudes and phases of the tides on the Bering Sea shelf. These waves, in a frictionless ocean, below the critical latitude, propagate as free waves; above this latitude they change to subinertial evanescent waves. The tide on the Bering Sea shelf along the Alaska Peninsula is determined by the barotropic Kelvin wave (Mofjeld, 1980). Kelvin wave exists both in subcritical and supercritical latitudes, and hence, this wave strongly influences the Bering Sea semidiurnal (superinertial) and diurnal (subinertial) tides.

This paper is organized in the following way. In Section 2, a simple set of the long-wave equations and boundary conditions is formulated in the dimensionless form. In Section 3, the natural frequency band for the Kelvin-like wave trapped around an island with a circular sill is defined. Oscillations are investigated for the subinertial frequency range. In Section 4, scattering of Sverdrup wave by an island is considered for a wide frequency range. The aim is to explore changes of the dipole over a large range of island dimensions and frequencies. Scattering of the Sverdrup wave by an island with a circular sill is examined in Section 5. Kelvin wave scattering by an island with a circular sill is presented in Section 6. Section 7 discusses the results and their application to the field observations.

Basic properties of the Sverdrup and Kelvin waves in an inviscid ocean are briefly discussed in Appendix A. In Appendix B, the wave propagation, subject to bottom friction, is considered. Appendix C describes components of matrix and vectors occurring in the wave scattering problem.

2. Basic equations and boundary conditions

In ensuing considerations, the dimensionless form of the long-wave equations of motion and the continuity equation will be used,

$$\frac{\partial \mathbf{u}}{\partial t} + \mathbf{k} \times \mathbf{u} = -\nabla \zeta - \frac{\gamma}{d} \mathbf{u}, \tag{1}$$

$$\frac{\partial \zeta}{\partial t} + \nabla \cdot (d\mathbf{u}) = 0, \tag{2}$$

where t is time, $\mathbf{u}$ is the vector of the horizontal velocity, ζ is the water surface elevation, $\mathbf{k}$ is the unit vector perpendicular to the ocean surface, ∇ is the differential operator, $\times$ denotes the vector product, dot denotes the scalar product, γ is the dimensionless bottom drag coefficient, and d is the dimensionless water depth.

Eqs. (1) and (2) are written in the vector form, which is the same both for Cartesian (x, y) and polar (r, θ) coordinate systems. These systems are related by formulas $x = r \cos \theta$, $y = r \sin \theta$ (r is the polar radius and θ is the polar angle). The components of the vector $\mathbf{u}$ in the rectangular and polar coordinate systems are denoted as (u, v) and (u_r, u_θ), respectively. The vector $\mathbf{k} \times \mathbf{u}$ has components ($-v$, u) and ($-u_\theta$, u_r) in these systems of coordinates.

Dimensional variables denoted by letters with stars are related to dimensionless variables in the following way,

$$(x*, y*) = \frac{\sqrt{gH_0}}{f} (x, y), \qquad t* = f^{-1}t, \qquad (u*, v*) = U(u, v), \qquad \zeta* = U\sqrt{\frac{H_0}{g}} \zeta,$$

$$(3)$$

where g is the gravity acceleration, H_0 is the typical water depth, and f is the Coriolis parameter, $d = H/H_0$, where H is the variable water depth. In this choice of the dimensionless variables the scaling for the horizontal coordinates is the Rossby radius, and for the time it is the Coriolis parameter. The sea level and velocity scaling are interconnected because (1) and (2) are linear and external forcing is absent. Thus the choice of the sea level will define the velocity scale U as well.

The nonlinear expressions for the bottom stress,

$$\frac{r}{H} u* \sqrt{u*^2 + v*^2} \quad \text{and} \quad \frac{r}{H} v* \sqrt{u*^2 + v*^2} \tag{4a}$$

have been linearized as,

$$\frac{C}{H} u* \quad \text{and} \quad \frac{C}{H} v* \tag{4b}$$

The dimensionless bottom drag coefficient γ is related to the coefficient C as $\gamma = C/(fH_0)$. We assume that $\mathbf{u}$ and ζ change periodically in time

$$\mathbf{u} = \mathbf{u}_0 e^{i\omega t}, \qquad \zeta = \zeta_0 e^{i\omega t}, \qquad \omega > 0. \tag{5}$$

Here ω is dimensionless angular frequency. Since the dimensionless time involves the Coriolis parameter (see (3)), the dimensional frequency $\omega*$ is expressed as $\omega* = \omega f$.

Introducing (5) into Eqs. (1) and (2) and assuming that $d = \text{const}$, we can obtain the equation for the sea level amplitude ζ_0,
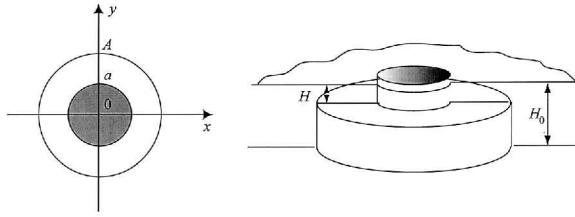
$$\Delta\zeta_0 + K^2\zeta_0 = 0, \tag{6}$$

Figure 2. Cylindrical island of radius a with a circular sill of radius A. Shallow water depth is H and the deeper water depth is H_0. The depth discontinuity is located at distance A from the origin.

where

$$K^2 = \frac{i\omega\Lambda}{\gamma + i\omega d}, \qquad \Lambda = -1 - \left(\frac{\gamma}{d} + i\omega\right)^2, \qquad \Delta = \nabla \cdot \nabla.$$

From (1) the components of velocity $\mathbf{u}_0$ in the Cartesian and polar coordinate systems are expressed through the sea level as

$$\Lambda u_0 = \left(\frac{\gamma}{d} + i\omega\right)\frac{\partial\zeta_0}{\partial x} + \frac{\partial\zeta_0}{\partial y}, \qquad \Lambda v_0 = \left(\frac{\gamma}{d} + i\omega\right)\frac{\partial\zeta_0}{\partial y} - \frac{\partial\zeta_0}{\partial x}, \tag{7a}$$

$$\Lambda u_{r,0} = \left(\frac{\gamma}{d} + i\omega\right)\frac{\partial\zeta_0}{\partial r} + \frac{1}{r}\frac{\partial\zeta_0}{\partial \theta}, \qquad \Lambda u_{\theta,0} = \left(\frac{\gamma}{d} + i\omega\right)\frac{1}{r}\frac{\partial\zeta_0}{\partial \theta} - \frac{\partial\zeta_0}{\partial r}. \tag{7b}$$

Propagation of the tides subject to scattering by the island will be investigated in the geometry plotted in Figure 2. The cylindrical island of the radius a is located at the center of the polar coordinates and is surrounded by the shallow water area limited by the circular sill. The distance from the center is defined by the radius vector $r = \sqrt{x^2 + y^2}$. The shallow area is located in the region $r \in (a, A)$. The depth discontinuity (sill) is located at $r = A$. Dimensional ocean depth, beyond the depth discontinuity ($r > A$) is equal to $H_0 =$ const, and within the shallow water area it is equal to $H = $ const ($H < H_0$) so, $d = 1$ at $r > A$ (in the deeper domain), and $d < 1$ at $r \in (a, A)$ (in the shallow water domain). The axes x and y of the rectangular system of coordinates are directed eastward and northward, respectively.

The matching boundary conditions relate the sea level and water transport across the depth discontinuity (Mei, 1989).

$$\lim_{r \to A-0} \zeta = \lim_{r \to A+0} \zeta, \tag{8a}$$

$$\lim_{r \to A+0} u_r = d \lim_{r \to A-0} u_r. \tag{8b}$$

At the island's coast, the normal velocity is zero,

$$u_r = 0, \qquad r = a. \tag{9}$$

Conditions (8b) and (9) can be reformulated using (7b) for applications in the polar coordinate system,

$$\lim_{r \to A+0} \left[(\gamma + i\omega) \frac{\partial \zeta_0}{\partial r} + \frac{1}{r} \frac{\partial \zeta_0}{\partial \theta} \right] = d \lim_{r \to A-0} \left[\left(\frac{\gamma}{d} + i\omega \right) \frac{\partial \zeta_0}{\partial r} + \frac{1}{r} \frac{\partial \zeta_0}{\partial \theta} \right] , \tag{10a}$$

$$\left(\frac{\gamma}{d} + i\omega \right) \frac{\partial \zeta_0}{\partial r} + \frac{1}{r} \frac{\partial \zeta_0}{\partial \theta} = 0, \qquad r = a. \tag{10b}$$

3. Kelvin-like trapped waves around a cylindrical island with a sill

The main target of our investigation is the island's response to the incident periodic waves. Such response is often defined by the proximity of the eigenperiods of the system and the periods of the incident waves. Therefore, the first step of the investigation is to use the free wave solutions of Eq. (6) to define a dispersion relation. This solution will be constructed from simple solutions for the cylindrical island derived in Appendix A (A.8b).

We pay the most attention to low (subinertial) frequency ($\omega < 1$ or $\lambda < 0$) waves propagating in the frictionless ocean ($\gamma = 0$). Numerical computations and field observations often reveal that subinertial trapped shelf waves of diurnal period play an important role in tidal dynamics (Huthnance, 1974; Hunkins, 1986; Chapman, 1989; Foreman *et al.,* 1993).

Solutions of Eq. (6) can be written in the following form

$$\zeta_0 = C^- K_n(\sqrt{-\lambda^-} r) e^{in\theta}, \qquad r > A,$$

for the outer region (beyond the sill), and

$$\zeta_0 = (C^+ K_n(\sqrt{-\lambda} r) + D^+ I_n(\sqrt{-\lambda} r)) e^{in\theta}, \qquad r \in (a, A), \tag{11}$$

for the inner region (over the sill). Here, K_n and I_n are Bessel functions, and $\lambda^- = \lambda|_{d=1}$ (see A.3).

Combining solutions for the inner and outer regions through the boundary conditions (8a), (10a) and (10b) yields the system of linear algebraic equations,

$$\mathbf{M}_n^1 \cdot \mathbf{l} = 0, \tag{12}$$

where components of the column vector $\mathbf{l}$ are C^-, C^+ and D^+.

The components of matrix $\mathbf{M}$ (Appendix C) depend on the frequency ω of the incident wave, the azimuthal number n, the relative depth d, the radius of the island a and the radius of the sill A. The system (12) has a non-zero solution when

$$\det \mathbf{M}_n^1 = 0. \tag{13}$$

Condition (13) defines the dispersion relation between frequency ω and the azimuthal wave number n of the free wave progressing around a cylindrical island with a surrounding sill.
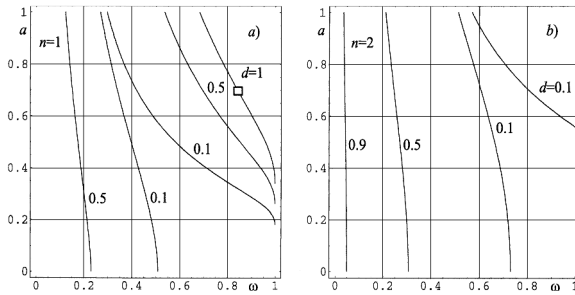
Figure 3. Eigenfrequency ω of the waves trapped around an island of the radius a, and sill radius $A = 2a$, constructed for different relative depth $d = H/H_0$. (a) First azimuthal mode, and (b) second azimuthal mode.

These Kelvin-like trapped waves propagate around the island and exponentially decay oceanwards from the island. Calculations show that (13) has real solutions only if $n > 0$. Therefore, in the northern hemisphere, all these trapped waves propagate clockwise around an island with a sill, exactly the same way as in the case of a cylindrical island without a sill (LeBlond and Mysak, 1978).

The eigenfrequencies of these trapped waves ω are plotted as a function of the island radius a, in Fig. 3a for the first ($n = 1$), and in Figure 3b for the second ($n = 2$) azimuthal modes. Longuet-Higgins (1969) demonstrated that only trapped waves of the first azimuthal mode ($n = 1$) occur around an island without a surrounding sill. This case follows from the above equation when the depth is constant $d \to 1$ (see Fig. 3a). Dispersion curves of the second azimuthal mode $n = 2$ tend to the vertical axis $\omega = 0$ when $d \to 1$, precluding resonance response around the island without the sill.

Fig. 3a also demonstrates that Longuet-Higgins' (1969) trapped waves ($n = 1$, $d = 1$) occur in the vicinity of the island with the dimensionless radius $a > 0.33$. In the dimensional form, that means that $a_d > 0.33\sqrt{gH_d}/f$. If $H \approx 25$ m, $f \approx 10^{-4}$ s^{-1} it follows that $a_d > 50$ km. Therefore, these waves can exist for larger radii only.

The wave frequency ω as a function of the depth d, is given in Figure 4a for the sill radius $A = 1.3a$, and in Figure 4b for $A = 2a$. Azimuthal numbers n are also shown in these figures. The radius of the island is $a = 0.04$. These dimensionless parameters are related to the following set of dimensional parameters; $f = 1.22 \times 10^{-4}$ s^{-1}, $H = 80$ m and $a_d = 10$ km, which is close to the parameters of the Pribilof Islands. The depth contrast between the outer (deep) and inner (shallow) domains influences the distribution of the eigenfrequencies, both for the smaller (Fig. 4a) and larger (Fig. 4b) islands in similar fashion. The smaller relative depth ($d \to 0$) corresponds to the greater frequency of the system. It is obvious that only oscillations related to the first and second azimuthal modes are distinctive enough to be observed.

In summary, Figures 3 and 4 show the wide range of eigenmodes in the subinertial frequency range $\omega \in (0, 1)$. A more complicated geometry of the island with the
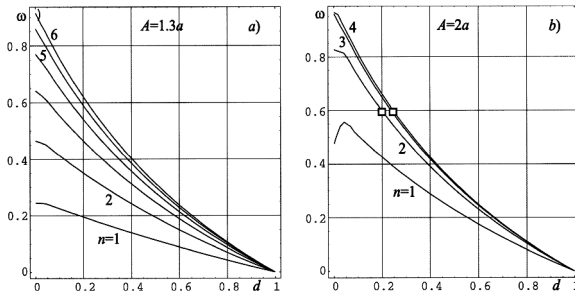
Figure 4. Eigenfrequency ω as a function of the relative depth d for the different azimuthal modes (n), island radius is $a = 0.04$. (a) The sill radius $A = 1.3a$, and (b) the sill radius $A = 2a$.

surrounding sill stipulates existence of a wider range of eigenfrequencies and the possibility of trapped waves around smaller and larger islands. A large portion of this frequency range is associated with the diurnal tides. Assuming that the O_1 has the longest period in the diurnal range ($T_{O_1} = 25.81$ h), the frequency range of the diurnal tides is $\omega \in (0.46, 1)$. It occurs poleward from the critical latitudes.

Having defined the general dispersion relation given by (13) for the island with the sill, it is possible to consider the dispersion equation for the free waves over a cylindrical seamount as the case when the radius of the island $a \rightarrow 0$. As has been demonstrated by Huthnance (1974), Hunkins (1986), and Chapman (1989), the free waves over a seamount are responsible for enhancement of diurnal tides. The dispersion equation (13) when $a \rightarrow 0$ is given in Figure 5a for three azimuthal modes ($n = 1, 2, 3$) as a function of the parameter $d(A = 0.1)$. The ratio of the depth over the seamount plateau to the depth at the base of the seamount defines d. The solution which describes trapped subinertial waves is constructed from the wave C in region $r > A$ and from the wave D in region $r < A$. Amplitudes of the C and D waves are related, since $CK_n(\sqrt{-\lambda^-}A) = DI_n(\sqrt{-\lambda}A)$. Kelvin-like trapped waves display the maximum amplitude in the vicinity of the depth discontinuity at $r = A$.
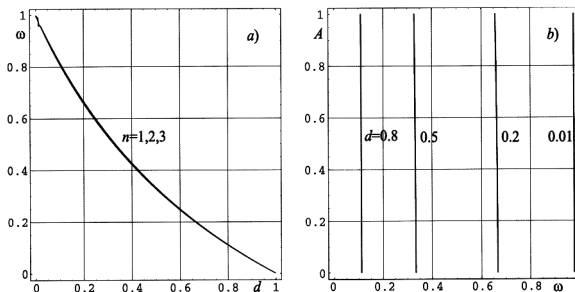

Figure 5. (a) The eigenfrequency ω of the waves trapped around a seamount of the radius $A = 0.1$ as function of the relative depth $d = H/H_0$. (b) The eigenfrequency ω as function of A for the different d.

Their analog in the rectangular system of coordinates are double-Kelvin waves traveling along rectilinear (Longuet-Higgins, 1968) and periodical (Kasajima and Marchenko, 2001) depth discontinuities.

Frequency ω of the first azimuthal mode ($n = 1$) as a function of the wide range of seamount sizes (radius A) for different values of d is shown in Figure 5b. For the given d, the frequency of the first azimuthal mode is nearly independent of the radius of the seamount plateau. Thus, seamounts of the various horizontal dimensions will have very close eigenfrequencies as long as the depth contrast between plateau and base remains the same. This result supports the ideas of Hunkins (1986) and Chapman (1989), that the amplification at the diurnal tides can occur over a wide range of seamount sizes.

The dispersion relations considered above are constructed for the simple geometry of a cylindrical seamount with vertical walls or for a cylindrical island with a circular sill bounded by vertical walls. The analysis of oscillations trapped around islands and seamounts with a smooth depth profile performed by Rhines (1969) indicates that additional slow oscillations (topographic Rossby waves) occur in that case. For the cylindrical island and seamount with vertical walls, these modes are absent.

4. Scattering of a Sverdrup wave by an island

The total amplitude of sea level oscillations around an island will be given by the sum of the complete set of the orthogonal functions—solutions of Eq. (6), see Appendix A. It is convenient to consider incident waves in the Cartesian coordinate system and scattered waves in the polar coordinate system (Proudman, 1914; Longuet-Higgins, 1967). Longuet-Higgins (1967, 1969) investigated propagation of long gravity waves in the vicinity of the cylindrical island, neglecting the influence of the Coriolis force. Lee and Kim (1999) extended previous investigations by neglecting the term $K^2\zeta_0$ in Eq. (6) and introducing bottom friction. This approximation is reasonable provided the wavelength is large compared with the radius of the island. We abandon this approximation, but more importantly we consider the wide range of frequencies and island sizes to investigate patterns of the sea level in the scattered wave around the island. This will allow us to determine the uniqueness of the dipole structure observed for the tides in the Barents and Bering seas and in Tsushima Strait. The water surface elevation due to the incident Sverdrup wave propagating along the x-axis (eastward) in the water body of the constant depth ($d = 1$) can be described as

$$\zeta_i = e^{i(\omega t - k_x x)} = \sum_{n=-\infty}^{\infty} i^n J_n(-k_x r) e^{i(n\theta + \omega t)}, \tag{14}$$

where $k_x = K|_{d=1}$ and $\omega > 1$. For the frictionless ocean ($\gamma = 0$) the incident wave of unit amplitude remains the same for the entire domain. Due to bottom friction, the amplitude of the incident wave varies, therefore, at the center of the island the amplitude of the incident wave is set to unity.

Water surface elevation induced by the scattered wave is given by the sum of the radial D-waves (see A.8a) which decreases outward from the island

$$\zeta_s = \sum_{n=-\infty}^{\infty} B_n H_n^{(2)}(k_x r) e^{i(n\theta + \omega t)}. \tag{15}$$

Introducing the sea level, $\zeta = \zeta_i + \zeta_s$, as the sum of incident and scattered waves, into the boundary condition at the island perimeter (8b) and assuming $d = 1$, we can define the coefficient B_n in (15) as,

$$B_n = -i^n \frac{\omega \dfrac{\partial J_n(-k_x a)}{\partial a} + \dfrac{n}{a} J_n(-k_x a)}{\omega \dfrac{\partial H_n^{(2)}(k_x a)}{\partial a} + \dfrac{n}{a} H_n^{(2)}(k_x a)}. \tag{16}$$

Using asymptotic formulas for the large azimuthal numbers $n \gg r$,

$$J_n(r) \approx \frac{1}{2} \sqrt{\frac{2}{\pi \nu}} \exp\left(\nu - n \operatorname{arctanh} \frac{\nu}{n} \right), \qquad H_n^{(2)}(r) \approx i \sqrt{\frac{2}{\pi \nu}} \exp\left(-\nu + n \operatorname{arctanh} \frac{\nu}{n} \right) ,$$

the basic term in (15) can be estimated as,

$$B_n H_n^{(2)}(Kr) \approx \frac{iKa}{2\sqrt{2}\pi} \left[\left(\frac{eK^2 a^2}{2} \right)^4 \frac{2}{eK^2 r^2 n^2} \right]^n , \qquad n \gg r,$$

which assures convergence of (15). Here e is the Euler number, and $\nu = \sqrt{n^2 - r^2}$.

Observations of the M_2 changes around Bear Island, Barents Sea (Kowalik and Proshutinsky, 1995), around the Pribilof Islands, Bering Sea (Kowalik and Stabeno, 1999), and around Cheju Island, sea of Japan (Lee and Kim, 1999) show the dipole structure in the tidal amplitude distribution around these islands. It is possible to demonstrate that the dipole structure, or more generally, the number of extrema in the sea level amplitude distribution depends on the frequency of the incident wave and the relative size of the island. Figure 6 presents results of several numerical experiments aimed at investigating the influence of various parameters (island radius, frequency, bottom friction, etc.) on the pattern of the sea level extrema.

To be able to connect our results with the Longuet-Higgins (1969) high frequency waves around the island, a wide range of island sizes (radius a) and a wide range of wave frequencies ω is considered. Figure 6 shows changes with time of local sea level extrema around the island perimeter, in the frictionless ocean ($\gamma = 0$) for the same $\omega = \omega_{sd}$ (semidiurnal), but for different a (Fig. 6a–c), for the same a but for $\omega = 10\omega_{sd}$ (Fig. 6d), and for $\omega = 40\omega_{sd}$ (Fig. 6e). The extrema progress almost clockwise around the island when the frequency of the incident wave is close to the inertial frequency f (Figs. 6a, b, and c). Increasing the frequency ω of the incident wave is associated with the increasing of time
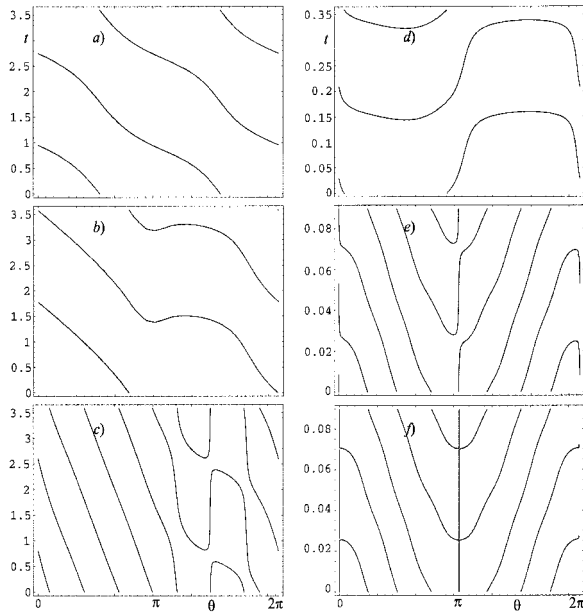
Figure 6. Trajectories of the local extrema of the sea level along the perimeter of a cylindrical island constructed for the incident Sverdrup wave. Horizontal axis denotes the polar angle θ, vertical axis denotes time t. The following parameters are used: (a) $\omega = \omega_{sd} = 1.75$ and $a = 0.074$, (b) $\omega = \omega_{sd}$ and $a = 0.5$, (c) $\omega = \omega_{sd}$ and $a = 2$, (d) $\omega = 10\omega_{sd}$ and $a = 0.074$, (e) $\omega = 40\omega_{sd}$ and $a = 0.074$, (f) $f = 0$, $\omega = 40\omega_{sd}$ and $a = 0.074$.

intervals of the counterclockwise motion (Figs. 6d, e, and f). At high frequencies the clockwise and counterclockwise motions of extrema are almost equal (Fig. 6e). In this case, the sea level is almost symmetric relative to the line $x = 0$. The case considered by Longuet-Higgins (1969) is given in Figure 6f. In this case the water elevation is symmetric relative to the line $x = 0$. Since isolines in Figure 6e and Figure 6f are very similar, we can conclude that the derived solution asymptotically tends to the Longuet-Higgins solution when $\omega \to \infty$. The number of the extrema of sea levels around the island's perimeter increases with increasing wave frequency ω and radius of the island a. There are only two extrema in the Figures 6a and d. Figure 6b shows mainly two extrema, but during short time intervals four extrema exist. There are up to eight extrema in Figures 6c, e, and f.

Sea level extrema in all these figures display the eigenstructure of trapped waves around an island and the interaction of this structure with the incident wave. The dipole pattern in the sea level distribution is expressed by one azimuthal wave number, therefore it is the lowest mode of oscillations which generally displays the strongest response to the applied random forcing. Field observations show that this mode occurs for a wide range of periods; it was more strongly excited by the M_2 wave but it occurs also at the diurnal period. The quadrapole appears less frequently in the above figures. It shows two maxima and two
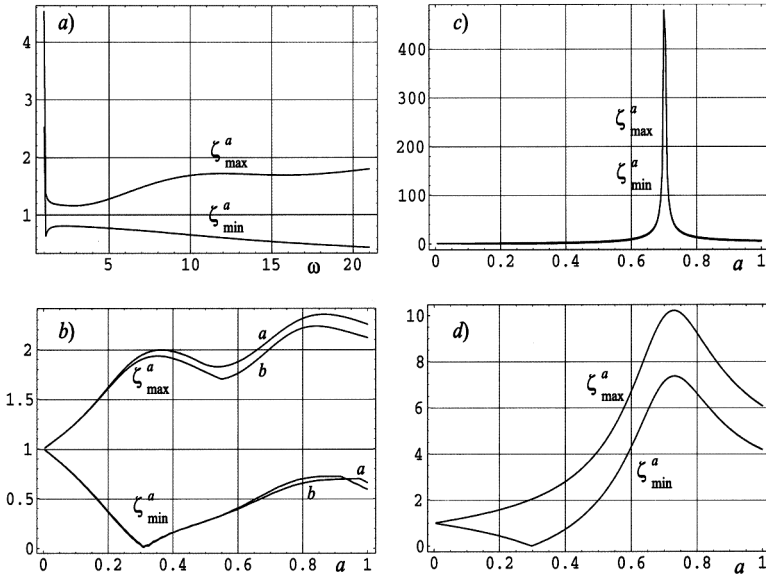
Figure 7. Maximum ζ^a_{max} and minimum ζ^a_{min} of sea level amplitudes along the island perimeter as a function of: (a) frequency ω, and (b, c, d) radius of the island a. The following parameters are used: (a) $a = 0.074$, $\gamma = 0$; (b) $\omega = \omega_{sd} = 1.75$, $\gamma = 0.176$ (lines a), $\gamma = 0$ (lines b); (c) $\omega = \omega_d = 0.84$, $\gamma = 0$; and (d) $\omega = \omega_d = 0.84$, $\gamma = 0.176$.

minima, therefore these oscillations are expressed by the second mode of the azimuthal oscillations.

These experiments reveal that the local sea level extrema can be quite useful as a tool for investigations of the trapped tidal motion around islands. For this purpose let us define the maximum of sea level elevation at each point (x, y) as

$$\zeta_{max} = \max_{t \in (0, 2\pi/\omega)} \zeta. \tag{17}$$

From (5) it follows that $\zeta_{max} = |\zeta_0|$, therefore it denotes the wave amplitude. Quantities ζ^a_{max} and ζ^a_{min},

$$\zeta^a_{max} = \max_{\theta \in (0, 2\pi)} \zeta_{max}|_{r=a},$$
$$\zeta^a_{min} = \min_{\theta \in (0, 2\pi)} \zeta_{max}|_{r=a}, \tag{18}$$

define the maximum and minimum of the wave amplitude along the island perimeter during one cycle.

Parameters ζ^a_{max} and ζ^a_{min} as functions of frequency in the superinertial range ($\omega > 1$) are plotted in Figure 7a. The radius of the island is $a = 0.074$ and the bottom friction is set to zero $\gamma = 0$. As one would expect in the absence of friction very large values of ζ^a_{max} and ζ^a_{min} occur in the proximity of $\omega = 1$. We approach this limit and find the amplitude distribution as $\omega \to 1$. Leblond and Mysak (1978) pointed out that this trapped motion

remains unbounded at large distances from the island. However, at the island the first mode of oscillations remains bounded and the boundary conditions for the velocity are also fulfilled.

The influence of the island radius on the pattern of minimum and maximum of the sea level amplitude at the semidiurnal frequency $\omega = \omega_{sd}$ is depicted in Figure 7b. The following parameters are considered: $\gamma = 0.176$ (lines a) and $\gamma = 0$ (lines b). Around small islands ($0 < a < 0.3$), the maximum amplitude ζ_{max}^a increases and the minimum amplitude ζ_{min}^a decreases monotonically. Both ζ_{max}^a and ζ_{min}^a tend to the amplitude of the incident wave (unit value) when $a \to 0$. The behavior of these functions, in the region $a > 0.3$, becomes more complicated due to the increased number of the local extrema along the island perimeter. From this figure one quite obvious result follows, namely that the maximum of the total amplitude around an island is always greater than the amplitude of the incident wave. Although we do not present the details of the solution for the scattering problem for the incident wave of diurnal period, some results are given in Fig. 7c ($\gamma = 0.$) and 7d ($\gamma = 0.176$). Due to resonance between the incident wave and the eigenoscillations (depth $d = 1$) discussed in Section 3, a strong maximum in both ζ_{max}^a and ζ_{min}^a occurs for the radius $a = 0.7$. This resonant point is marked by a square in Figure 3a. The influence of resonance is especially conspicuous for the frictionless case (Fig. 7c), however it also influences motions subject to bottom friction. Although in the latter case, the amplification is much smaller compared to the frictionless ocean, the range of the island radius over which resonance occurs significantly increases (Fig. 7d). When $a < 0.3$, the magnitudes of ζ_{max}^a are slightly greater for the semidiurnal tide than for the diurnal tide, and the magnitudes of ζ_{min}^a are slightly smaller for the semidiurnal tide than for the diurnal tide.

Finally, we present the amplitude and phases around the island constructed by solving the scattering problem for the semidiurnal and diurnal Sverdrup waves (Figs. 8 and 9). To compare the results of our calculations with those by Lee and Kim (1999), we used the following parameters: $f = 0.8 \cdot 10^{-4}\,\text{s}^{-1}$ (latitude 33°20′N), $H = 75$ m, and $a_d = 25$ km. These results compare well with the distribution given by Lee and Kim, 1999 (see Fig. 4). Certain differences are related to the direction of propagation of the incident waves: eastward in our computations and westward in computations by Lee and Kim (1999).

5. Scattering of a Sverdrup wave by an island with a circular sill

All results presented in the previous section were obtained for a simple model of a circular island without a shelf. However, it is well known (LeBlond and Mysak, 1978) that shelves significantly modify the existing modes and introduce new types of eigenmodes. Therefore, we carried out several numerical experiments to examine the interaction of the incident Sverdrup wave with an island surrounded by a circular sill. The geometry of this problem is given in Figure 2. Water surface elevation is described by (14) in the outer domain $r > A$. The amplitude of the incident wave is taken to be equal 1 at $x = 0$. The presence of bottom friction results in changes in the incident wave amplitude, therefore the
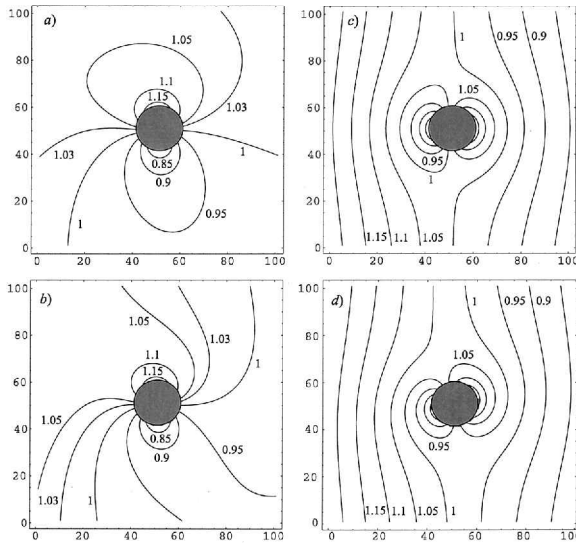
Figure 8. Amplitudes of the semidiurnal ($\omega = \omega_{sd} = 1.75$) (a, b), and diurnal ($\omega = \omega_d = 0.84$) (c, d) tides induced by the Sverdrup wave around the island of the radius $a = 0.074$. (a) and (c) without bottom friction, and (b) and (d) with bottom friction, $\gamma = 0.176$.
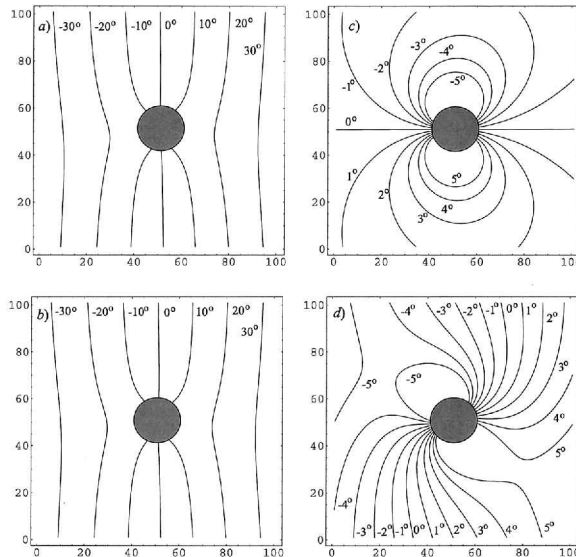

Figure 9. Phases of the semidiurnal (a, b) and diurnal (c, d) Sverdrup waves. (a) and (c) no bottom friction, and (b) and (d) with bottom friction $\gamma = 0.176$.

amplitude at $x = 0$ is used to determine the incident wave distribution around the island when bottom friction is included. In the ensuing consideration we discuss the solution for the viscous ocean.

In the deeper domain (see Fig. 2) the solution can be constructed as

$$\zeta = \zeta_i + \zeta_s^-, \qquad r > A; \tag{19a}$$

and in the shallower domain as

$$\zeta = \zeta_s^+, \qquad r \in (a, A), \tag{19b}$$

where $\zeta_s^\pm$ denotes scattered waves.

Using (19) the scattered wave in the shallower domain can be constructed as a sum of the outgoing signal reflected from the island and the incoming signal from the depth discontinuity and the deep ocean (see B.5, B.6),

$$\zeta_s^+ = \sum_{n=-\infty}^{\infty} (C_n^+ H_n^{(1)}(K^+ r) + D_n^+ H_n^{(2)}(K^+ r)) e^{i(n\theta + \omega t)}, \tag{20a}$$

where $K^+ = K|_{d<1}$ (see Appendix B).

The scattered wave in the deeper domain consists of an outgoing signal reflected from the depth discontinuity,

$$\zeta_s^- = \sum_{n=-\infty}^{\infty} D_n^- H_n^{(2)}(K^- r) e^{i(n\theta + \omega t)}. \tag{20b}$$

After substituting (19) and (20) into boundary conditions (8b) and (10), and equating the terms with the same azimuthal number n, we get the system of linear algebraic equations to match solutions for the sea level and transport at the island perimeter and at the depth discontinuity (sill):

$$\mathbf{M}_n^2 \cdot \mathbf{l}_n = \mathbf{N}_n, \tag{21}$$

where the components of the column vector $\mathbf{l}_n = (C_n^+, D_n^+, D_n^-)$. The components of 3×3 matrix $\mathbf{M}_n^2$ and column vector $\mathbf{N}_n$ are rational functions of the functions $H_n^{(1)}(K^\pm r)$, $H_n^{(2)}(K^\pm r)$, and their first derivatives at the points $r = a$ and $r = A$. The components of 3×3 matrix $\mathbf{M}_n^2$ and column vector $\mathbf{N}_n$ are defined in Appendix C.

The solution of the system (21) for every n defines constants C_n^+, D_n^+ and D_n^-. By introducing these constants into (19) and (20), we define the water surface elevation in the entire domain.

To describe the tide distribution around the Pribilof Islands the following parameters have been used in our numerical calculations

$$f = 1.22 \times 10^{-4}\, s^{-1}, \quad a_d = 10\, km, \quad H_0 = 80\, m, \quad \omega_{sd} = 1.15, \quad \omega_d = 0.596. \tag{22}$$
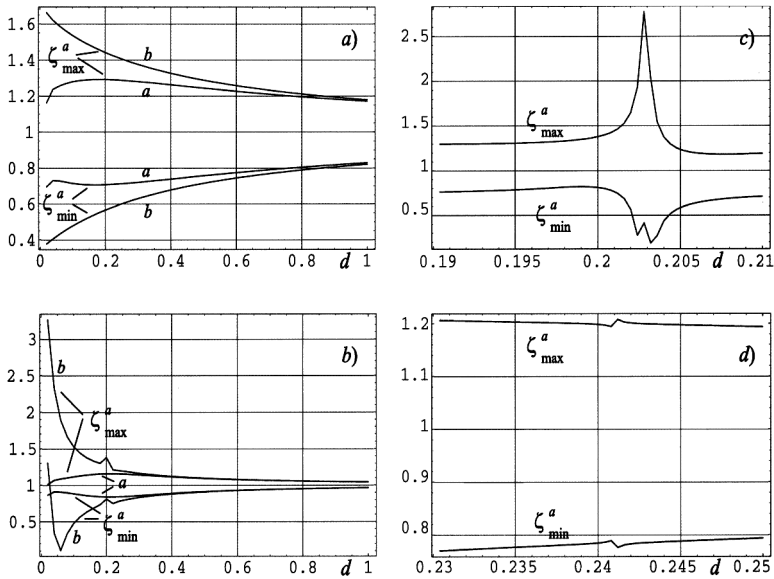
Figure 10. Maximum ζ_{max}^a and minimum ζ_{min}^a of sea level amplitudes along the island perimeter as a function of the relative depth d ($A = 2a$, $a = 0.043$), induced by the Sverdrup wave. (a) $\omega = \omega_{sd} = 1.15$, and (b, c, d) $\omega = \omega_d = 0.596$. Lines marked by letter a are related to ($\gamma = 0.064$), and by letter b to $\gamma = 0$. (c) Describes resonance with the second and (d) resonance with the third azimuthal modes.

As we did before to investigate sea level changes around the island, we use the maximum and minimum amplitude at the island perimeter. Maximum ζ_{max}^a and minimum ζ_{min}^a of the water level amplitude are plotted as a function of the relative depth d in Figure 10. This series of experiments involves a wider sill with the depth discontinuity located at $A = 2a$. The coefficient of the linear bottom friction is calculated by $\gamma = rU/(H_0 f)$, where $r = 2.5 \times 10^{-3}$ and velocity is $U = 0.25$ cm s^{-1}. Figure 10a describes the semidiurnal tide ($\omega = \omega_{sd}$). The bottom friction significantly damps the wave amplitude near the island when the relative depth is smaller than 0.4 (in the shallow domain the depth is approximately 30 m). If this depth increases, the influence of the friction becomes less important.

Figure 10b describes diurnal tide ($\omega = \omega_d$). The wave amplitude is significantly reduced due to the bottom friction in the shallow water when the depth is smaller than 0.2. Comparison of Figs. 10a and 10b along the perimeter of the island shows that amplitudes of the semidiurnal tide are smaller than the amplitudes of the diurnal tides for small relative depth, while for larger depth ($d > 0.5$) the semidiurnal tides dominate over the diurnal tides.

Figures 10c and 10d show the enhanced picture of the resonance effect for the diurnal tide as seen in Figure 10b in proximity to $d = 0.2$. The origin of this resonance was shown
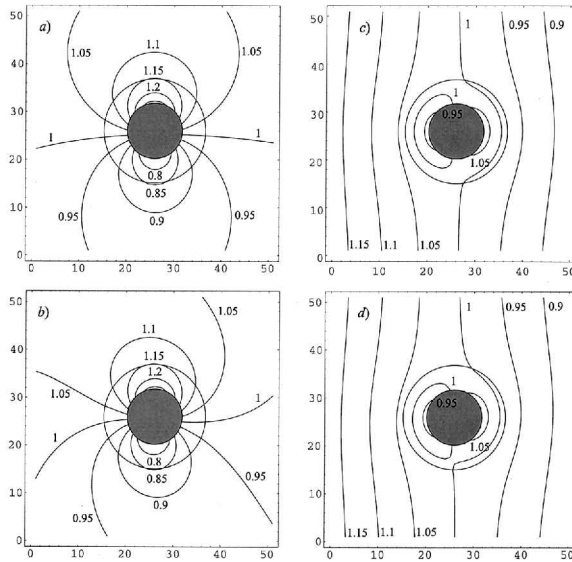
Figure 11. Amplitudes of the semidiurnal ($\omega = \omega_{sd} = 1.15$) (a, b), and diurnal ($\omega = \omega_d = 0.596$) (c, d) tides induced by the Sverdrup wave around the island with the circular sill ($a = 0.043$, $A = 2a$). (a) and (c) without bottom friction, and (b) and (d) with bottom friction, $\gamma = 0.064$.

in the Figure 4. At the latitude of the Pribilof Islands the diurnal frequency $\omega_d = 0.596$ can be used to locate resonance modes as a function of the relative depth and the radius of the sill. Diurnal incident wave impinging on the island with the small sill (Fig. 4a) can excite only the third azimuthal mode of the eigenoscillations while on the island with the larger-size sill (Fig. 4b) the second and third modes are excited (marked by squares in Fig. 4b). It is of interest to see that resonance with the lowest modes ($n = 1, 2$ in Fig. 4a, and $n = 1$ in Fig. 4b) is absent for the Pribilof Islands. As seen in Figure 10b, omission of bottom friction has strongly influenced the wave amplitude in the vicinity of the resonance. The peaks in Figures 10c, and d occur only over the very narrow range of the relative depth d, this implies that the resonance modes are difficult to excite.

A series of experiments was carried out to investigate the role of the sill width in the total amplitude distribution generated by the incident Sverdrup wave. In Figure 11 and in Figure 12 the amplitudes and phases are given for the radius of the sill $A = 2a$ and in Figures 13 and 14 the amplitudes and phases are given for the narrower sill $A = 1.3a$. The scale of Figures 11 and 13 is 1:0.008, i.e. the length of the interval between two ticks in the frame is equal to 0.008 in the dimensionless space.

The four distributions given in Figures 11 and 13 show that signal enhancement is stronger for the semidiurnal frequencies of oscillations than for diurnal frequencies. For both ranges of periods we consider the same geometry. Therefore, the differences can be explained from the properties of the amplitude response given in Figure 10. Indeed, from this figure the conclusion is that the amplitudes at the island perimeter for the relative depth
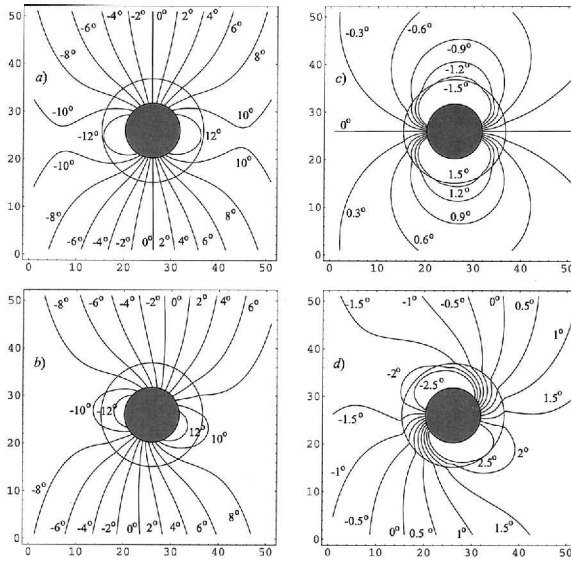
Figure 12. Phases of the semidiurnal (a, b) and diurnal (c, d) Sverdrup waves. (a) and (c) no bottom friction, and (b) and (d) with bottom friction $\gamma = 0.064$. All parameters as in Figure 11.
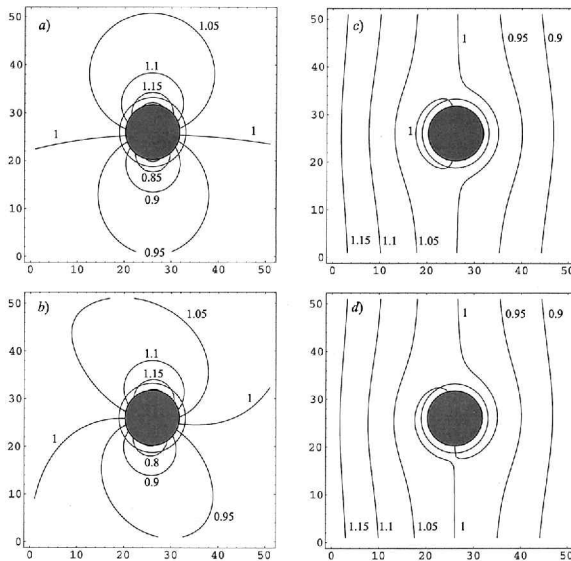

Figure 13. Amplitudes of the semidiurnal ($\omega = \omega_{sd} = 1.15$) (a, b), and diurnal ($\omega = \omega_d = 0.596$) (c, d) tides induced by the Sverdrup wave around the island with the circular sill ($a = 0.043$, $A = 1.3a$, $d = 0.5$). (a) and (c) without bottom friction, and (b) and (d) with bottom friction, $\gamma = 0.064$.
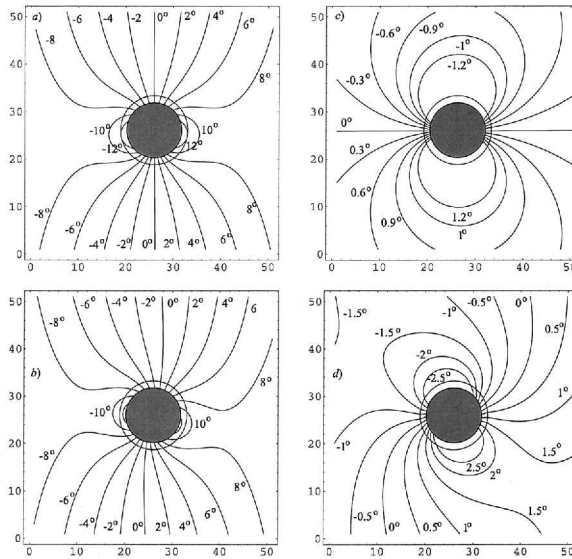
Figure 14. Phases of the semidiurnal (a, b) and diurnal (c, d) Sverdrup waves. (a) and (c) no bottom friction, and (b) and (d) with bottom friction $\gamma = 0.064$. All parameters as in Figure 13.

$d = 0.5$ are enhanced stronger at semidiurnal than at diurnal periods. Experiments for the two sill radii ($A = 2a$ in Figs. 11 and $A = 1.3a$ in Fig. 13) show that both semidiurnal and diurnal tide amplitudes have increased in the vicinity of the island due to the increased radius of the sill. The phase differences (Figs. 12 and 14) across the island also increase for the wider sill. The phase difference across the island (Fig. 12) is much larger for the semidiurnal wave, the time difference (without bottom friction) for the semidiurnal wave is 0.8 h and for the diurnal wave it is 0.2 h. These phase differences show that the wave progresses around the sill much faster than around the island and has different speeds at different locations around the island perimeter.

The previous computations of the sea level amplitude distribution around an island and around an island with a circular sill enables us to estimate the influence of frequency and sill geometry on the amplitude distribution. The presence of the sill changes the amplitude distribution. Figure 11 is constructed for St. Paul Island, i.e. for an island of 10 km radius with a circular sill ($A = 20$ km), while an island of 25 km radius (Cheju Island) is considered in Figure 8. Although in the latter case the radius of the island is larger than in the former case, the maximum amplitude around the smaller island is greater than around the bigger island. This larger amplitude is caused by the influence of the circular sill around St. Paul Island.

We had started our investigation in Section 1 hoping that around an island or an island with a sill the trapped diurnal mode would occur. Generally, as can be gleaned from Figures 8 and 11, the diurnal Sverdrup wave (being a subinertial evanescent mode) is

poorly enhanced compared to the semidiurnal wave. The evanescent behavior is clearly seen in Fig. 11 which shows the amplitude attenuation from west to east. Nonetheless, the possibility for diurnal resonance is clearly given: a) for an island without a sill the peak is at $a \approx 0.7$, and b) for an island with a sill the peak is at $d = 0.2$.

6. Scattering of a Kelvin wave by an island with a circular sill

In this section we investigate the response of an island with a circular sill to the unit amplitude incident Kelvin wave which propagates along x-direction. The water surface elevation for this wave is described as

$$\zeta_i = e^{i(\omega t - k_x x + k_y y)} = \sum_{n,m=-\infty}^{\infty} i^n (-i)^{n-m} J_m(-k_x r) J_{n-m}(k_y r) e^{i(n\theta + \omega t)}, \tag{23}$$

where complex numbers k_x and k_y are related through formula (B.2). As in the previous section the solution is constructed for the viscous ocean.

The solution in the outer (deeper) domain $r > A$ and the inner (shallower) domain $r \in (a, A)$, is described by formulas (19) and (20) in which the incident wave ζ_i is defined by (23). Introducing (19), (20), and (23) into the boundary conditions (8), (9), and (10), and equating terms with the same azimuthal number n, we obtain the following system of the linear algebraic equations:

$$\mathbf{M}_n^2 \cdot \mathbf{l}_n = \mathbf{N}_n^1, \tag{24}$$

where components of the vector $\mathbf{N}_n^1$ are defined in Appendix C.

Solving system (24) for each azimuthal number n we find constants C_n^+, D_n^+, and D_n^-. By inserting these constants into (19) and (20) we can define the water surface elevation at every point of the surface (x, y). The location and the radius of the island are defined by (22).

First, we shortly examine the possibility of resonance for the subinertial frequency range by computing total amplitude around the island with the sill due to the incident diurnal Kelvin wave. The maximum and minimum of the sea level amplitude (ζ_{max}^a and ζ_{min}^a) along the island perimeter as a function of the relative depth d is given in Figure 15. These plots are similar to those obtained for the Sverdrup wave (Fig. 10b), the frictionless motion (lines b) shows enhanced wave amplitudes for the small relative depth ($d < 0.2$) and near $d = 0.2$, due to the resonance of the incident wave at the frequency of the second azimuthal mode of the eigenoscillations (see Fig. 4b). This is the same frequency that occurred for the Sverdrup wave response. The bottom friction strongly damps the wave amplitudes for the small relative depth and in the vicinity of the resonance frequency. The response functions for the Kelvin wave (Fig. 15) and for the Sverdrup wave (Fig. 10b) show a subtle differences in the behaviors of these waves. In particular at the local
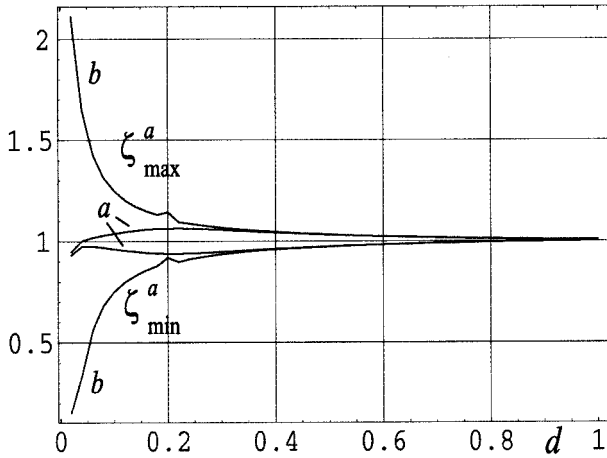
Figure 15. Maximum ζ^a_{max} and minimum ζ^a_{min} of sea level amplitudes along the island perimeter as a function of the relative depth d ($A = 2a$, $a = 0.043$), induced by the diurnal Kelvin wave ($\omega = \omega_d = 0.596$). Lines marked by letter a are related to ($\gamma = 0.064$), and by letter b to $\gamma = 0$.

maximum $d = 0.2$, the maximum for the Kelvin wave is significantly smaller than the Sverdrup wave maximum.

We use the above equations to investigate the total amplitude generated by the incident diurnal Kelvin wave. The responses for the smaller ($A = 1.3a$) and wider ($A = 2a$) sills are explored. The amplitude given in Figure 16 shows that the larger sill tends to induce a slight enhancement of the amplitude in comparison to the smaller sill.

The phase distribution in Figure 17, illustrates a similar result, i.e., the effects of the wave scattering around the island with the sill are stronger for the larger sill.

A comparison with the previous experiments enables us to conclude that under identical conditions (i.e., the geometry and physics of the problem) the scattering effects due to the Sverdrup wave dominate the scattering effects caused by the Kelvin wave. Investigations of the total amplitude due to the incident semidiurnal Kelvin wave, (although we do not present the computational results), reveal similar relations between the scattered effects in the Kelvin and Sverdrup waves.

7. Discussions and conclusions

The main purpose of the present study was to examine and to explain certain peculiarities of the tidal variations around two islands of approximately identical diameter in the Bering Sea. These peculiarities testify to the existence of waves trapped by these islands and shelves, which form a dipole structure rotating clockwise around the islands.

The basic facts can be summarized in the following: (1) Observations and numerical modeling show specific peculiarities in the amplitude and phase distribution both for semidiurnal and diurnal tides. These peculiarities are stronger for semidiurnal tides. (2)
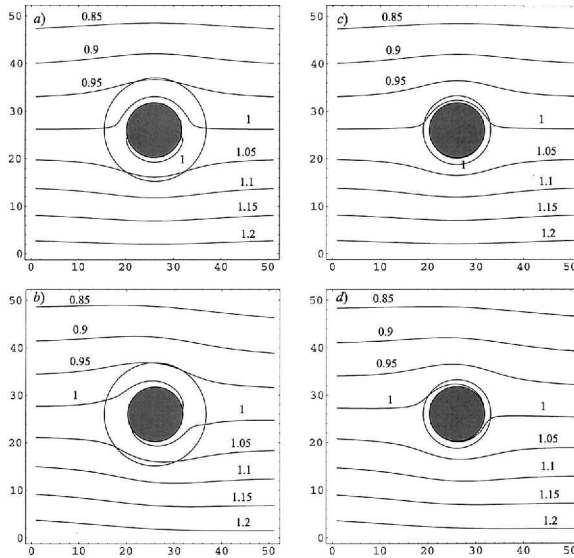
Figure 16. Amplitude of the and diurnal ($\omega = \omega_d = 0.596$) tide induced by the Kelvin wave around the island with the circular sill ($a = 0.043$, $d = 0.5$). (a) and (b) $A = 2a$, and (c) and (d) $A = 1.3a$. (a) and (c) no bottom friction, and (b) and (d) with bottom friction $\gamma = 0.064$.
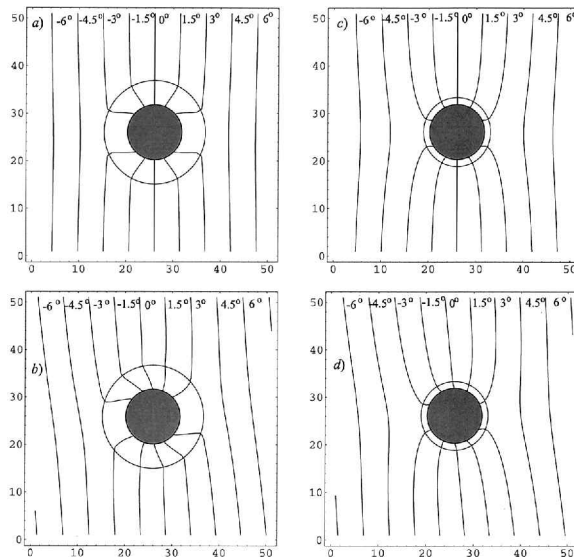

Figure 17. Phase of the diurnal Kelvin wave. All parameters as in Figure 16.

Local sea level and phase contrasts are stronger across the northern island (St. Paul) than across the southern island (St. George).

In our approach we assumed that these peculiarities were related to the trapping effects around the islands and to the interaction of the incident waves with the islands. The constructed model of an island in the ocean of a constant depth was found to be insufficient to explain the behavior of tidal waves in the region of the Pribilof Islands. However, the inclusion of a sill changed the situation. The "skirt" around the Pribilof Islands was found to play an important role in formation of the observed tidal peculiarities. The differences between diurnal and semidiurnal tides are found to be associated with: (a) different incident waves for these two types of tides, and (b) different eigenmodes. Computations of the island and circular sill response to the incident Sverdrup and Kelvin waves demonstrate that the former produces a more pronounced dipole structure and phase contrast for the semidiurnal wave and wider sill around the island. Kelvin waves and diurnal Sverdrup waves do not appear to have much effect on tidal waves around the islands.

These computations show that the dominant response is in the semidiurnal frequency band with a stronger response at the northern island due to the wider domain of the shallow water surrounding this island. An additional question to be answered is how this general picture is changed in the case of resonance response? Of special interest is the response in the subinertial frequency band due to influence of the topographic Rossby waves trapped around the islands (Rhines, 1969). If these modes of oscillations could be excited around the island, this would result in trapped waves similar in nature to the trapped shelf waves which strongly affect diurnal tides in high latitudes (Hunkins, 1986; Kowalik and Proshutinsky, 1995; Rabinovich and Thomson, 2001). Calculations point out that the resonance indeed could occur in certain situations, in particular for the large-diameter islands and for the wider and shallower sill.

To explain the differences between the Pribilof Islands we constructed a model including the shelf surrounding the islands, and the problem is formulated as the scattering of the arriving tidal waves by an island with a sill. In this investigation, we have chosen to study the behavior of Sverdrup incident waves which are scattered into Kelvin-like waves trapped around an island. Numerical experiments for a typical island radius of 10 km and sill radii of 13 km and 20 km, show much stronger enhancement of the semidiurnal oscillations compared to the diurnal oscillations. The enhancement is a function of the sill width, showing stronger amplification for the wider sill. These results explain the different amplifications of the M_2 tide observed around St. Paul and St. George islands in the Bering Sea. Could we actually repeat the textbook statement that: "the strength of the scattered signal is also a function of the wavelength, since the wavelengths of the incident diurnal and semidiurnal waves are different, the stronger scattering effect will occur for the shorter wavelength (shorter period)." Not quite, because the frictionless response around the island investigated through the maximum amplitude at the island perimeter (Fig. 10) shows strong dependence on the relative depth as well; at small relative depths ($d \rightarrow 0$) the

diurnal response dominates, while at larger relative depths ($d \geq 0.2$) the semidiurnal response is stronger.

Obviously, the different enhancement of the Sverdrup and Kelvin waves is related to the different basic properties of these waves as described briefly in Appendix A. Free Sverdrup waves play the key role in the formation of semidiurnal tides, while Kelvin waves influence both semidiurnal and diurnal tides. To explain the role of the Sverdrup wave in the formation of the diurnal tides we can invoke the bottom friction (Lee and Kim, 1999) or the evanescent mode which shows significant spatial attenuation.

In the semidiurnal frequency range, the observations and numerical computations of the M_2 wave trapped around an island show that from the point of view of an observer looking in the propagation direction of the incident wave, the tidal amplitude increases to the left and decreases to the right of the island. The incident Kelvin wave, from the point of view of the same observer, will feature the opposite sea level slope; the amplitude decreases from the right to the left. As Lee and Kim (1999) pointed out, the amplitude variation of the incident Kelvin wave along the perimeter of the island is compensated for by the scattered wave amplitude. Thus, the sum of the incident wave amplitude and the response amplitude in the Kelvin wave is much smaller compared to the total change caused by the incident Sverdrup wave.

In the diurnal frequency band, the Sverdrup wave generates a relatively small scattered signal. This behavior can be caused by significant damping of the incident wave in the subinertial frequency band. The difference between the Kelvin and Sverdrup waves in the diurnal band is best demonstrated by the different response of the sea level around an island in a shallow water domain (Fig. 10b and Fig. 15). While resonance is possible for both waves due to the peak at the $d = 0.2$, the maximum sea level for the Kelvin wave reaches only 1.15, while for the Sverdrup wave the maximum is 1.35.

The interactions of incident waves with islands could cause a resonance in the case of coincidence of the incident wave frequencies with the eigenfrequencies of the trapped waves propagating around the island. In the examined cases the diurnal oscillations depict a strong maximum at $a \approx 0.7$ but otherwise the response is flat, while the semidiurnal oscillations have a more complicated dependence on the radius. A strong resonance response of the diurnal mode, can occur for larger islands. At the latitude of St. Paul Island, Bering Sea ($57°20'$N) and at the average depth of 80 m, the nondimensional radius $a = 0.7$ is equivalent to the radius of 160 km. However the observed radius of St. Paul Island is approximately 10 km.

A sill probably plays a key role in explanation of the observed peculiarities of the tidal behavior. It produces a new type of trapped waves which did not occur around an island with vertical walls, i.e., high frequency gravity waves and low-frequency topographic waves. It also produces additional modes of eigenoscillations which are important for resonance with incident waves. It produces additional bottom friction in the shallow inner region around the island, which plays an important role in the wave modification. The presence of a sill around the island leads to two possible responses in the tidal range of

oscillations. While diurnal tides (due to resonance interaction) are amplified at the relative depth ($d \simeq 0.2$); the semidiurnal tides are amplified at the large relative depth ($d > 0.5$). Examination of the entire range of frequencies shows that the resonance excitation of the diurnal tide at $d = 0.2$ is caused by the second and third azimuthal modes of eigenfrequencies. The resonance strongly depends on the depth contrast between shallower and deeper domains surrounding the island. For the depth in the outer domain of $H_0 = 80$ m, the waves in the shallow inner domain ($H = 0.2H_0 = 16$ m) will be affected by strong bottom friction which will result in the strong damping of the resonance response (see Fig. 10b). Additionally, this mode occurs over a very narrow range of the relative depth variations d, implying that the resonance mode is quite difficult to excite.

Field observations and numerical computations show that the most frequent pattern of the tidally trapped sea level change around an island is the dipole structure, which rotates clockwise around an island. We have related this pattern to the first azimuthal mode of the Kelvin-like waves trapped around an island. Because this is the lowest mode of oscillations one would expect that it displays the strongest response to the forcing and very stable behavior. Measurements reveal that this pattern occurs over a wide range of frequencies and therefore it can not be limited to the resonance excitation only. To investigate the dipole structure, a wide range of frequencies and the island's dimensions have been considered. The results show that the dipole structures occur in proximity to the tidal frequency band when islands are small relative to the barotropic Rossby radius. This scaling depends both on the latitude and on the depth. At the latitude of St. Paul Island, Bering Sea the nondimensional radius $a = 0.5$ is equivalent to the radius of 114 km when depth is 80 m, and it is equal to 57.3 km when depth is 20 m. Two extrema (one maximum and one minimum) of the sea level occur around a small island (radius less than 0.5) at the semidiurnal frequency band. Waves of the same frequency around much bigger islands (radius $a \geq 2$) have up to eight extrema. Thus, the main reason that the dipole structure occurs at the tidal frequency is the relatively small size of the islands. Patterns of the local extrema of the sea level amplitude for the higher frequency waves show increasing numbers of maxima and minima, and their rotation is both clockwise and counterclockwise. For the shorter wave periods, the results of the present study are in good agreement with those obtained by Longuet-Higgins (1969), yielding validation of the technique used in this investigation.

APPENDIX A

Wave propagation without bottom friction

Neglecting the effect of the bottom friction, we consider a periodic along the x-direction solution of Eq. (6) when $d = $ const (constant depth). Assuming sea level as,

$$\zeta_0 = \exp(-ik_x x)\eta_0(y), \qquad k_x > 0 \tag{A.1}$$

a simple equation for η_0 follows,

$$\frac{d^2\eta_0}{dy^2} = -k_y^2\eta_0, \tag{A.2}$$

wherein

$$k_y^2 = \lambda - k_x^2, \ \lambda = \left.\frac{\Lambda}{d}\right|_{\gamma=0} = \frac{\omega^2 - 1}{d}. \tag{A.3}$$

defines the dispersion relation (LeBlond and Mysak, 1978). The solution of (A.2) is

$$\eta_0 = A \ \exp(ik_y y) + B \exp(-ik_y y). \tag{A.4}$$

The wave number k_y is real if $\lambda > k_x^2$, and it takes an imaginary value if the reverse inequality holds. Further, the part of solution (A.4) proportional to A is called wave A, and the part proportional to B is called wave B.

Waves with the real wave numbers k_y are called the Sverdrup waves. The limiting frequency for Sverdrup waves is $\omega = f$ (Sverdrup, 1926). Poleward of the critical latitude the free Sverdrup wave becomes an exponentially decaying. Since the above is in the dimensionless form, we can bring back the dimensional variables through transformation (3), thus, introducing the dimensional wave number κ_{xd} and frequency ω_d, the above inequality can be rewritten as,

$$\left(\frac{\omega_d}{f}\right)^2 > 1 + \left(\frac{k_{xd}\sqrt{(gH)}}{f}\right)^2. \tag{A.5}$$

For the imaginary wave number k_y, from (A.3) for the given frequency ω and wave number k_x two wave numbers are possible: $k_y^+ = i((1 - \omega^2)/d + k_x^2)^{1/2}$ and $k_y^- = -k_y^+$. Let us consider $k_y = k_y^+$. In this case the wave A is left-decreasing and the wave B is right-decreasing from the point of view of an observer looking along the positive x axis. Waves of type A are called Kelvin waves (Platzman, 1971). At the critical latitude $\omega = 1$ ($\omega_d = f$) water velocities u_0 and v_0 in the Kelvin wave have no singularities, while singularity occurs in the Sverdrup wave.

The free wave solutions of equation (6) in the polar coordinate system can be constructed in the following way (LeBlond and Mysak, 1978),

$$\zeta_0 = \exp(in\theta)\eta_n(r) \tag{A.6}$$

where θ is polar angle, r is radius, and n is integer number. The Bessel equation for η_n follows,

$$\frac{\partial^2 \eta_n}{\partial r^2} + \frac{1}{r}\frac{\partial \eta_n}{\partial r} + \left(\lambda - \frac{n^2}{r^2}\right)\eta_n = 0. \tag{A.7}$$

Solution of equation (A.7) takes the form

$$\eta_n = CH_n^{(1)}(\sqrt{\lambda}r) + DH_n^{(2)}(\sqrt{\lambda}r), \qquad \lambda > 0, \tag{A.8a}$$

$$\eta_n = CK_n(\sqrt{-\lambda}r) + DI_n(\sqrt{-\lambda}r), \qquad \lambda < 0, \tag{A.8b}$$

where $H_n^{(1)} = J_n + iY_n$ and $H_n^{(2)} = J_n - iY_n$. For future reference we will call the above solution the wave C, if $D = 0$, and the wave D, if $C = 0$. At the critical latitude ($\omega = 1$) the water velocities $u_{n,r}$ and $u_{n,\theta}$ in the wave C are continuous, and in the wave D are discontinuous.

APPENDIX B

Wave propagation subject to bottom friction

Assuming the dependent variables change periodically in time, we can present the spatial dependence of (6) as,

$$\zeta_0 = Ae^{i(-k_x x + k_y y)} + Be^{i(-k_x x - k_y y)}. \tag{B.1}$$

As before, the wave propagates along the positive x direction, but due to the bottom friction the wave number k_x is no longer real and positive, but complex. Therefore, $k_x = \Re k_x + i\Im k_x$ ($\Re k_x > 0$), and $k_y = \Re k_y + i\Im k_y$.

Substituting (B.1) into equation (6) we get

$$k_x^2 + k_y^2 = K^2. \tag{B.2}$$

The part of solution (B.1) proportional to A will be called wave A, and the part proportional to B will be called wave B. If $k_y = 0$ the difference between waves A and wave B cease to exist. The waves A and B coincide with the Sverdrup wave running along x direction for the frictionless case $\gamma = 0$ and $\omega > 1$. If $\gamma > 0$ then the complex wave number of the Sverdrup wave becomes equal to K. Simple algebraic calculations show that the real and imaginary parts of K have different signs. Assuming

$$\Re K > 0, \qquad \Im K < 0, \tag{B.3}$$

it follows that the Sverdrup wave is exponentially decreasing at the large values of x. If $\omega < 1$ and the coefficient of bottom friction γ tends to zero, wave A tends to the Kelvin wave. The wave numbers for the wave propagation subject to bottom friction were defined by Lee and Kim (1999).

To investigate the role of friction in the polar coordinate system let us consider the free

wave solutions of equation (6). Assuming the form of the free wave as in (A.6), the Bessel equation for η_n follows,

$$\frac{\partial^2 \eta_n}{\partial r^2} + \frac{1}{r}\frac{\partial \eta_n}{\partial r} + \left(K^2 - \frac{n^2}{r^2}\right)\eta_n = 0. \tag{B.4}$$

Solution of the equation (B.4) takes the form

$$\eta_n = CH_n^{(1)}(Kr) + DH_n^{(2)}(Kr), \tag{B.5}$$

Asymptotes of η_n for large values r are given by formulas

$$\eta_n \sim \frac{C}{r}\exp\left(i\left(Kr - \left(\frac{n}{2}+\frac{1}{4}\right)\pi\right)\right) + \frac{D}{r}\exp\left(-i\left(Kr - \left(\frac{n}{2}+\frac{1}{4}\right)\pi\right)\right). \tag{B.6}$$

From (B.3) and (B.6) it follows that the wave D decays at the large values of r; on the other hand, the wave C is exponentially increasing when $r \to \infty$.

APPENDIX C

Components of matrixes $\mathbf{M}_n^1$, $\mathbf{M}_n^2$ and vectors $\mathbf{N}_n$, $\mathbf{N}_n^1$

$$M_{n,11}^1 = \omega \frac{\partial I_n(\sqrt{-\lambda}a)}{\partial a} + \frac{n}{a}I_n(\sqrt{-\lambda}a), \qquad M_{n,12}^1 = \omega \frac{\partial K_n(\sqrt{-\lambda}a)}{\partial a} + \frac{n}{a}K_n(\sqrt{-\lambda}a),$$

$$M_{n,13}^1 = 0,$$

$$M_{n,21}^1 = I_n(\sqrt{-\lambda}A), \qquad M_{n,22}^1 = K_n(\sqrt{-\lambda}A), \qquad M_{n,23}^1 = -K_n(\sqrt{-\lambda^-}A),$$

$$M_{n,31}^1 = d\omega \frac{\partial I_n(\sqrt{-\lambda}A)}{\partial A} + \frac{dn}{A}I_n(\sqrt{-\lambda}A), \qquad M_{n,32}^1 = d\omega \frac{\partial K_n(\sqrt{-\lambda}A)}{\partial A} + \frac{dn}{A}K_n(\sqrt{-\lambda}A),$$

$$M_{n,33}^1 = \omega \frac{\partial K_n(\sqrt{-\lambda^-}A)}{\partial A} + \frac{n}{A}K_n(\sqrt{-\lambda^-}A).$$

$$M_{n,11}^2 = \left(\frac{\gamma}{d}+i\omega\right)\frac{\partial H_n^{(1)}(Ka)}{\partial a} + \frac{in}{a}H_n^{(1)}(Ka),$$

$$M_{n,12}^2 = \left(\frac{\gamma}{d}+i\omega\right)\frac{\partial H_n^{(2)}(Ka)}{\partial a} + \frac{in}{a}H_n^{(2)}(Ka),$$

$$M_{n,13}^2 = 0, \qquad M_{n,21}^2 = H_n^{(1)}(KA), \qquad M_{n,22}^2 = H_n^{(2)}(KA), \qquad M_{n,23}^2 = -H_n^{(2)}(K^-A),$$

$$M_{n,31}^2 = \left(\frac{\gamma}{d}+i\omega\right)\frac{\partial H_n^{(1)}(KA)}{\partial A} + \frac{in}{A}H_n^{(1)}(KA),$$

$$M_{n,32}^2 = \left(\frac{\gamma}{d}+i\omega\right)\frac{\partial H_n^{(2)}(KA)}{\partial A} + \frac{in}{A}H_n^{(2)}(KA),$$

$$M_{n,33}^2 = \left(\frac{\gamma}{d} + i\omega\right) \frac{\partial H_n^{(2)}(K^-A)}{\partial A} + \frac{in}{A} H_n^{(2)}(K^-A), \qquad N_{n,1} = 0, \qquad N_{n,2} = i^n J_n(-K^-A),$$

$$N_{n,3} = i^n\left(\frac{\gamma}{d} + i\omega\right) \frac{\partial J_n(-K^-A)}{\partial A} + i^n \frac{in}{A} J_n(-K^-A).$$

$$N_{n,1}^1 = 0, \quad N_{n,2}^1 = i^n \sum_{m=-\infty}^{\infty} (-i)^{n-m} J_m(-k_x A) J_{n-m}(k_y A)$$

$$N_{n,3}^1 = i^n \sum_{m=-\infty}^{\infty} (-i)^{n-m}\left(\frac{\gamma}{d} + i\omega\right) \frac{\partial J_m(-k_x A) J_{n-m}(k_y A)}{\partial A} + \frac{in}{A} J_m(-k_x A) J_{n-m}(k_y A).$$

REFERENCES

Chapman, D. C. 1989. Enhanced subinertial diurnal tides over isolated topographic features. Deep-Sea Res., *36,* 815–824.

Defant, A. 1960. Physical Oceanography, Pergamon Press, *2,* 598 pp.

Foreman, M. G. G., R. F. Henry, R. A. Walters and V. A. Ballantyne. 1993. A finite element model for tides and resonance along the north coast of British Columbia. J. Geophys. Res., *98,* 2509–2532.

Hunkins, K. 1986. Anomalous diurnal tidal currents over the Yermak Plateau. J. Mar. Res., *44,* 51–69.

Huthnance, J. M. 1974. On the diurnal tidal currents over Rockwall Bank. Deep-Sea Res., *21,* 23–35.

Kantha, L. H. 1995. Barotropic tides in the global oceans from a nonlinear tidal model assimilating altimetric tides. 1. Model description and results. J. Geophys. Res., *100,* 25,283–25,308.

Kasajima, Y. and A. Marchenko. 2001. On the excitation of resonant double Kelvin waves in the Barents Sea Opening. Polar Res., *20,* 241–248.

Kowalik, Z. 1999. Bering Sea Tides, *in* The Bering Sea: Physical, Chemical and Biological Dynamics, T. R. Loughlin and K. Ohtani, eds., Alaska Sea Grant Press, Fairbanks, AK, 93–127.

Kowalik, Z. and A. Yu. Proshutinsky. 1995. Topographic enhancement of tidal motion in the western Barents Sea. J. Geophys. Res., *100,* 2613–2637.

Kowalik, Z. and P. Stabeno. 1999. Trapped motion around the Pribilof Islands in the Bering Sea. J. Geophys. Res., *104,* 25,667–25,684.

Larsen, J. C. 1977. Cotidal charts for the Pacific Ocean near Hawaii using *f*-plane solutions. J. Phys. Oceanogr., *7,* 100–109.

LeBlond, P. H. and L. A. Mysak. 1978. Waves in the Ocean, Elsevier, 602 pp.

Lee, S. H. and K. Kim. 1993. Scattering of a Kelvin Wave by a cylindrical island. J. Oceanogr. Soc. Korea, *28,* 177–185.

—— 1999. Scattering of tidal frequency waves around a cylindrical island. J. Phys. Oceanogr., *29,* 436–448.

Loder, J. W. 1980. Topographic rectification of tidal currents on the sides of Georges Bank. J. Phys. Oceanogr., *10,* 1399–1416.

Longuet-Higgins, M. S. 1967. On the trapping of wave energy round islands. J. Fluid Mech., *29,* 781–821.

—— 1968. On the trapping of waves along a discontinuity of depth in a rotating ocean. J. Fluid Mech., *31,* 417–434.

—— 1969. On the trapping of long-period waves round islands. J. Fluid Mech., *37,* 773–784.

Mei, C. C. 1989. The Applied Dynamics of Ocean Surface Waves. World Scientific, 740 pp.

Mofjeld, H. O. 1980. Effects of vertical viscosity on Kelvin waves. J. Phys. Oceanogr., *10,* 1039–1050.

—— 1984. Recent observations of tides and tidal currents from the northeastern Bering Sea shelf. NOAA Tech. Memo. ERL PMEL-57, PMEL, Seattle, 36 pp.

Pearson, C. A., H. O. Mofjeld and R. B. Tripp. 1981. Tides of the Eastern Bering Sea shelf, *in* The Eastern Bering Sea Shelf: Oceanography and Resources, D. W. Hood and J. A. Calder, eds., US Dept. of Commerce, 111–130.

Platzman, G. W. 1971. Ocean tides and related waves, *in* Mathematical Problems in the Geophysical Sciences. Amer. Math. Soc., Providence, RI, 239–291.

Proudman, J. 1914. Diffraction of tidal waves on flat rotating sheets of water. Proc. Lond. Math. Soc., *14,* 89–102.

Rabinovich, A. B. and R. E. Thomson. 2001. Evidence of diurnal shelf waves in the satellite-tracked drifter trajectories off the Kuril Islands. J. Phys. Oceanogr., *31,* 2651–2668.

Rhines, P. B. 1969. Slow oscillations in an ocean of varying depth. Part 2. Islands and seamounts. J. Fluid Mech., *37,* 191–205.

Sünderman, J. 1977. The semidiurnal principal lunar tide M_2 in the Bering Sea. Deutsche Hydrog. Zeitschrift, *30,* 91–101.

Sverdrup, H. W. 1926. Dynamics of tides on the North-Siberian shelf. Geofys. Publ. Norske Videnskaps-Akad., Oslo, *4,* 1–75.